ESA Contract AO/1-9322/18/I-NB

ESA Climate Change Initiative Extension
Aerosol-CCI+

Algorithm Theoretical Basis Document

Prepared by : M. Luffarelli, Y. Govaerts and L. Franceschini

Reference : Aerosol_cci+_ATBD_CISAR_SLSTR_V1.2
Version : V1.2

rayference

Document Change Record

Doc. Version	**Date**	**CISAR Release**	**Remarks**
Version 1.0	November 2020	2.0	First released version
Version 1.1	February 2021	2.0	Second released version
Version 2.1	January 2022	2.2	Third released version. Updated Section 4.2.3, 5.2 and 6.1.

Table of Contents

List of Acronyms

AERONET	Aerosol Robotic Network
AOT	Aerosol Optical Thickness
ATBD	Algorithm Theoretical Basis Document
AU	Astronomical Unit
BHR	BiHemispherical Reflectance
BRF	Bidirectional Reflectance Factor
CISAR	Combined Inversion of Surface and AeRosol
CMa	Cloud Mask
COT	Cloud Optical Thickness
ECMWF	European Centre for Medium- Range Weather Forecasts
EQMPN	Equivalent Model Parameter Noise
ESA	European Space Agency
EVL	Pixel elevation
LSM	Land Sea Mask
LUT	Look-Up Table
OE	Optimal Estimation
OT	Optical Thickness
RPV	Rahman - Pinty - Verstraete BRF model
RTLS	Ross Thick/Li- Sparse
RTM	Radiation Transfer Model
SLSTR	Sea and Land Surface Temperature Radiometer
SRFP	Surface Pressure
SWD	Surface Wind Direction
SWS	Surface Wind Speed
TCO3	Total column Ozone
TCWV	Total Column Water Vapour
TOA	Top-Of-Atmosphere
VZA	Viewing Zenith Angle
SZA	Solar Zenith Angle

EXECUTIVE SUMMARY

This document describes the algorithm used to generate surface reflectance and aerosol optical thickness products from Sea and Land Surface Temperature Radiometer (SLSTR) observations. This algorithm relies on a joint retrieval of surface reflectance and aerosol/cloud optical thickness based on the inversion of a coupled surface-atmosphere radiative transfer model.

The forward model is explicitly solved during the inversion process, *i.e.*, it does not rely on precomputed solutions, allowing a continuous variations of the state variables in the solution space.

The retrieval scheme is based on an Optimal Estimation (OE) approach where the cost function accounts for the differences between the observations and the forward radiative transfer model, the retrieved state variables and their prior information and finally smoothness constraints on spatial, temporal and spectral variations of the state variables.

1 INTRODUCTION

This ATBD describes the CISAR algorithm that infers aerosol and cloud optical thicknesses and surface reflectance over land and sea surfaces from observations acquired by the SLSTR radiometer in the S1, S2, S3, S4, S5, S6μm bands. As the algorithm derives the total column aerosol and cloud optical thickness, it does not discriminate between tropospheric and stratospheric particles. This algorithm relies on a joint retrieval of surface reflectance and aerosol/cloud optical thickness based on the inversion of a coupled surface-atmosphere radiative transfer model (Govaerts and Luffarelli 2018).

FASTRE, the forward model included in the CISAR algorithm, is explicitly solved during the inversion process, *i.e.*, it does not rely on pre-computed solutions, allowing a continuous variation of the state variables in the solution space.

The retrieval scheme is based on an Optimal Estimation (OE) approach where the cost function accounts for the differences between the observations and the forward radiative transfer model, the retrieved state variables and their prior information and finally smoothness constraints on temporal and spectral variations of the atmospheric properties.

The proposed algorithm capitalizes on the accumulation of SLSTR observations to perform an angular sampling of the radiance field under various angular geometries. The temporal accumulation of data acquired under different illumination and viewing conditions is thus used to form a virtual multi-angular measurement system. SLSTR data are thus accumulated in the S1, S2, S3, S4, S5, S6 bands during a given period to form the measurement vector. The primary objective of this accumulation is to document the surface Bidirection Reflectance Factor (BRF). During this accumulation period, the surface reflectance properties are assumed temporally invariant. The inversion procedure takes place at the end of this accumulation period to retrieve the surface reflectance and the optical thickness in each band. CISAR implements a rigorous uncertainty propagation scheme accounting for all the sources of uncertainties in the input data and prior information up to the retrieved solution covariance matrices.

2 INSTRUMENT CHARACTERISTICS

Sentinel-3 is an Earth observation satellite constellation developed by the European Space Agency (ESA) in the framework of the Copernicus programme, formerly Global Monitoring for Environment and Security. To accomplish its objectives, Sentinel-3 uses different sensing instruments: SLSTR (Sea and Land Surface Temperature Radiometer), OLCI (Ocean and Land Colour Instrument), SRAL (SAR Altimeter), DORIS, and MWR (Microwave Radiometer). Sentinel-3A was launched on 16 February 2016, Sentinel-3B followed on 25 April 2018. Sentinel-3 satellites are polar orbiting, flying at an altitude of 815 km with a local equatorial crossing time of 10:00 am.

The main focus of this project will be the SLSTR instrument on-board S3A, which covers 9 spectral bands (0.55-12.0 μm) . However, in the framework of this project, only bands S1, S2, S3, S4, S5, S6μm are considered. The SLSTR radiometer uses two independent scan mirrors rotating in opposite directions each scanning at a rate of 200 scans per minute. Each scan measures two along track pixels of 1 km (four or eight pixels at 500 m resolution for visible/NIR channels and SWIR channels, respectively) simultaneously. The swath widths are equal to 1420 km (nadir) and 750 km (oblique). The dual view of the SLSTR instrument allows a revisit time of 1.9 days at the equator and 1.5 days at latitude higher than 30°. The designed lifetime of the instrument is 7.5 years. A complete description of the SLSTR instrument can be found on the ESA web page https://sentinel.esa.int.

3 FORWARD MODEL

3.1 Vertical structure

FASTRE, the forward model $y_m(\mathbf{x}, \mathbf{b}; \mathbf{m})$ simulates the Top-Of-Atmosphere (TOA) Bidirectional Reflectance Factor (BRF) as a function of the viewing and illumination angles, the spectral band $\tilde{\lambda}$, the state of the atmosphere and underlying surface. This model depends on the retrieved state variables $\mathbf{x}$, the model parameters $\mathbf{b}$ and finally the observation conditions. The independent parameters, such as the acquisition geometry or the spectral band, that determine these observation conditions are denoted $\mathbf{m}$. The radiative transfer equation is solved with the Matrix Operator Method (Fischer and Grassl 1984) optimised by Liu and Ruprecht (1996) for a finite number of quadrature points.

The FASTRE model is designed to simulate radiometer observations acquired with a spectral interval characterized by the spectral response of the processed radiometer. The gaseous transmittance in these intervals is precomputed and stored in look-up tables. All other operations are performed online, *i.e.*, during the inversion process. The model separates the single scattering contribution from the multiple scattering one. The multiple scattering contribution is solved in the Fourier space.

The forward model relies on the same atmospheric vertical structure as in Govaerts et al. (2010), *i.e.*, a three-level system containing two layers that are radiatively coupled (Figure 1). The lower level z_0 is the surface. Over land, surface reflectance is represented by the so-called RPV model which has four parameters (ρ_0, k, Θ, h), all wavelength dependent (Rahman et al. 1993). Over sea surface, the BRF is simulated with the Cox-Munk model as implemented in Vermote et al. (1997). The lower atmospheric layer L_a, ranging from level z_p to z_a contains the scattering particles. Molecular scattering and absorption are also taking place in that layer. The upper layer L_g, ranging from z_a to z_s is only subject to molecular absorption. The uncertainty of this model is estimated on Section 4.2.4.3.

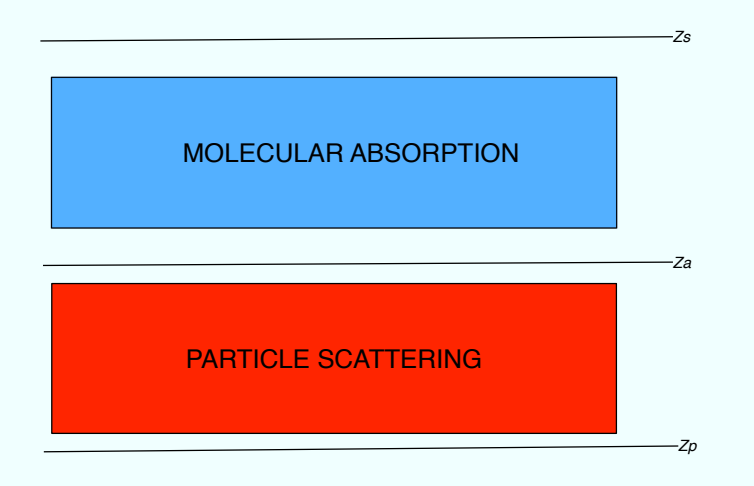

Figure 1: FASTRE forward model vertical structure. z_p is the pixel elevation at the surface, z_a is the height of the aerosol layer above z_p and z_s is the top of the gas absorption layer.

3.2 General mathematical formulation

The FASTRE model expresses the TOA BRF in a given spectral band $\tilde{\lambda}$ as a sum of the single $I_s^{\uparrow}$ and multiple $I_m^{\uparrow}$ scattering contributions as in

$$y_m(\mathbf{x},\mathbf{b};\mathbf{m}) \;=\; T_{L_g}(\mathbf{b};\mathbf{m})\;\frac{I_s^{\uparrow}(\mathbf{x},\mathbf{b};\mathbf{m}) \;+\; I_m^{\uparrow}(\mathbf{x},\mathbf{b};\mathbf{m})}{E_0^{\downarrow}(\mathbf{m})\mu_0} \tag{1}$$

where

$I_s^{\uparrow}(\mathbf{x},\mathbf{b};\mathbf{m})$ is the upward radiance field at level Z_a due to the single scattering;

$I_m^{\uparrow}(\mathbf{x},\mathbf{b};\mathbf{m})$ is the upward radiance field at level Z_a due to the multiple scattering;

$T_{L_g}(\mathbf{b};\mathbf{m})$ denotes the total transmission factor in the L_g layer;

$E_0^{\downarrow}(\mathbf{m})$ denotes the solar irradiance at level Z_s corrected for the Sun-Earth distance variations.

The single scattering contribution writes

$$I_s^{\uparrow}(\mathbf{x},\mathbf{b};\mathbf{m}) = \frac{E_0^{\downarrow}(\mathbf{m})\;\mu_0}{\pi}\exp\left(\frac{-\tau_{L_a}}{\mu_0}\right)\;r_s(\mathbf{x_s},\mathbf{b};\mathbf{m})\;\exp\left(\frac{-\tau_{L_a}}{\mu_v}\right) \tag{2}$$

where τ_{L_a} is the total optical thickness of layer L_a. μ_0 and μ_v are the cosine of the illumination and viewing zenith angles respectively.

The multiple scattering contribution $I_m^{\uparrow}(\mathbf{x},\mathbf{b};\mathbf{m})$ is solved in the Fourier space in all illumination and viewing directions of the quadrature directions N_θ for $2N_\theta - 1$ azimuthal directions. The contribution $I_m^{\uparrow}(\mathbf{x},\mathbf{b};\mathbf{m})$ in the direction (Ω_0,Ω_v) is interpolated from the surrounding quadrature directions.

3.3 Surface properties

3.3.1 Land surface

The surface reflectance at z_p is represented by the RPV model (Rahman et al. 1993) which has four parameters $\mathbf{x}_s = (\rho_0, k, \Theta, h)$, all wavelength dependent. The individual contribution of these four parameters to the total surface BRF is illustrated on Figure (2). Specifically,

- ρ_0 controls the mean amplitude of the BRF. This parameter strongly varies with the wavelength and mainly controls the mean surface reflectance. It varies between 0 and 1.
- k determines the bowl shape of the BRF. It varies between 0 and 2.
- Θ is the asymmetry parameter of the Henyey-Greenstein phase function and also varies between -1 and 1.
- h controls the amplitude of the hot-spot, *i.e.*, the "porosity" of the medium. This parameter takes only positive values and typically varies between 0 and 1.

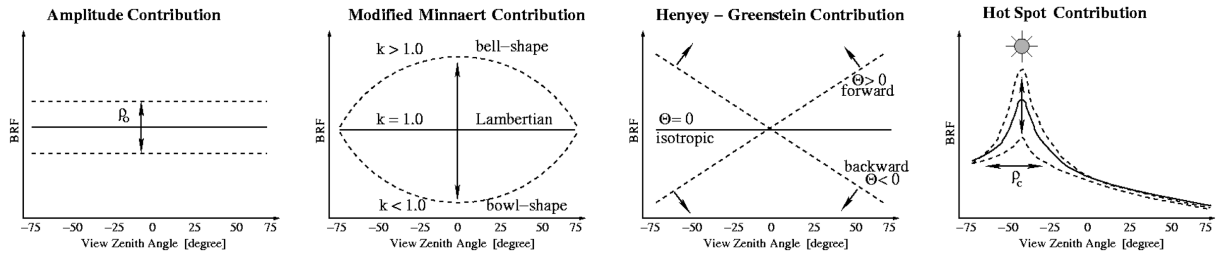

Figure 2: Contribution of the four RPV parameters to the total surface BRF.

Engelsen et al. (1996) analysed in detail on the performance and limits of applicability of this parametric model. The RPV model formally writes

$$r_s(\mathbf{x},\mathbf{b};\mathbf{m}) = \rho_0(\tilde{\lambda})\,\breve{\rho}_s(k(\tilde{\lambda}),\Theta(\tilde{\lambda}),h(\tilde{\lambda});\mu_0,-\mu_v,\phi_r) \tag{3}$$

where ρ_0 and $\breve{\rho}_s(k(\tilde{\lambda}),\Theta(\tilde{\lambda}),h(\tilde{\lambda});-\mu_v,\mu_0,\phi_r)$ describe the amplitude and the angular field of the surface BRF, respectively. This latter quantity is expressed by:

$$\breve{\rho}_s(k(\tilde{\lambda}),\Theta(\tilde{\lambda}),h(\tilde{\lambda});\mu_0,-\mu_v,\phi_r) = M_I(\mu_0,-\mu;k(\tilde{\lambda}))\,F(g;\Theta(\tilde{\lambda}))\,H(h(\tilde{\lambda});G) \tag{4}$$

where:

$$M_I(\mu_0,-\mu;k(\tilde{\lambda})) = \frac{\mu_0^{k-1}\mu^{k-1}}{(\mu_0+\mu_v)^{1-k}} \tag{5}$$

$$F(g;\Theta(\tilde{\lambda})) = \frac{1-\Theta^2(\tilde{\lambda})}{[1+2\Theta(\tilde{\lambda})\cos g+\Theta^2(\tilde{\lambda})]^{3/2}} \tag{6}$$

$$H(h(\tilde{\lambda});G) = 1+\frac{1-h(\tilde{\lambda})}{1+G} \tag{7}$$

$$\cos g = \cos\theta\cos\theta_0+\sin\theta\sin\theta_0\cos\phi_r \tag{8}$$

$$G = [\tan^2\theta_0+\tan^2\theta-2\tan\theta_0\tan\theta\cos\phi_r]^{1/2} \tag{9}$$

The relative azimuth angle, ϕ_r, is zero when the source of illumination is behind the satellite.

3.3.2 Sea surface

The total reflectance over sea surfaces is defined as being composed of three terms, representing three different sources of upwelling radiance fields. Firstly, light can be reflected off white caps in the rough ocean surface; secondly, it can be reflected off the sea surface itself. The relative contributions from these two factors will depend on the roughness of the sea surface, which is dependent on the surface wind speed v_{z_0}. Thirdly, light penetrating the surface can be scattered back up into the atmosphere by molecules within the water, such as water and dissolved pigments. Considering the combination of these terms, the sea surface reflectance in spectral band $\tilde{\lambda}$ writes

$$r_s(\mathbf{x},\mathbf{b};\mathbf{m}) = \rho_{wc}(v_{z_0};\tilde{\lambda})+(1-W)\rho_{gl}(v_{z_0};\tilde{\lambda})+(1-\rho_{gl}(v_{z_0};\tilde{\lambda}))\rho_{sw} \tag{10}$$

where

ρ_{wc} is the reflectance due to white caps

ρ_{gl} is the specular reflectance at the ocean surface

ρ_{sw} is the scattered reflectance emerging from sea water

W is the relative area covered with white caps

v_{z_0} is the surface wind speed.

The reflectance of the white cap is taken from Koepke (1984) and the specular contribution from Cox and Munk (1954). For the scattered reflectance emerging from sea water, a constant chlorophyll concentration of 0.1 [mg/m^3] is assumed (Morel 1988).

3.4 Scattering layer properties

The layer L_a contains a set of mono-mode aerosol and cloud classes v characterized by their single scattering properties, *i.e.*, the single scattering albedo $\omega_{0,v}(\tilde{\lambda})$ and phase function $\Phi_v(\tilde{\lambda}, \Omega_g)$ in the spectral bands $\tilde{\lambda}$ at the phase angle Ω_g. These classes define the vertices encompassing the solution space (Figure 3).

Concerning the aerosols, the different vertices representing fine and coarse mode are combined into this layer according to their respective optical thickness $\tau_v(\tilde{\lambda})$ with the total aerosol optical thickness (AOT) $\tau_a(\tilde{\lambda})$ of the layer being equal to

$$\tau_a(\tilde{\lambda}) = \sum_{v_a} \tau_{v_a}(\tilde{\lambda}) \tag{11}$$

In the same way, the total cloud optical thickness (COT) is computed combining the different vertices associated to water and ice clouds:

$$\tau_c(\tilde{\lambda}) = \sum_{v_c} \tau_{v_c}(\tilde{\lambda}) \tag{12}$$

The phase function $\Phi_v(\tilde{\lambda}, \Omega_g)$ of a vertex is characterized by a limited number N_κ of Legendre coefficients equal to $2N_\theta - 1$ where N_θ is the number of quadrature points used to solve the multiple scattering integral. The choice of this number results from a trade-off between accuracy and computer time. When N_κ is too small, the last Legendre moment is often not equal to zero and the delta-M approximation is applied (Wiscombe 1977). In that case, the α_d coefficient of the delta-M approximation is equal to $\Phi_v(N_\kappa)$. The Legendre coefficients κ_j, after application of the delta-M approximation, become

$$c_j = \frac{\kappa_j - \alpha_d}{1 - \alpha_d} \tag{13}$$

and the truncated phase function denoted Φ'_v. The corrected optical thickness $\tau'_v(\tilde{\lambda})$ and single scattering albedo $\omega'_{0,v}(\tilde{\lambda})$ of the corresponding class become

$$\tau'_v(\tilde{\lambda}) = (1 - \omega_{0,v}\alpha_d)\,\tau_v(\tilde{\lambda}) \tag{14}$$

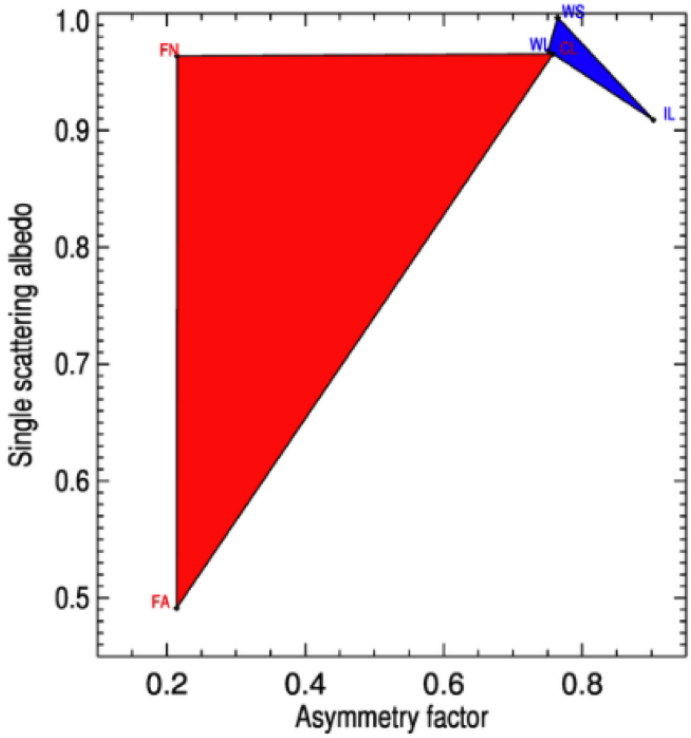

Figure 3: Aerosol and cloud single scattering properties at 1600nm in the asymmetry – single scattering albedo solution space. In this example, the aerosol solution space (red) is delineated by three vertices: Fine mode weakly absorbing (FN), fine mode absorbing (FA), coarse mode (CL). The cloud solution space is delineated by three vertices: Small drop water cloud (WS), large drop water cloud (WL) and large ice crystal (IL).

and

$$\omega'_{0,v}(\tilde{\lambda}) = \frac{1-\alpha_d}{1-\omega_{0,v}\alpha_d}\,\omega_{0,v}(\tilde{\lambda})\ . \tag{15}$$

The layer total optical thickness, τ_{L_a}, is the sum of the gaseous, τ_g, the aerosol, τ'_a, the cloud, τ'_c and the Rayleigh, τ_r, optical depth

$$\tau_{L_a}(\tilde{\lambda}) = \tau_g(\tilde{\lambda}) + \tau'_a(\tilde{\lambda}) + \tau'_c(\tilde{\lambda}) + \tau_r(\tilde{\lambda}) \tag{16}$$

with $\tau'_a(\tilde{\lambda}) = \sum_v \tau'_v(\tilde{\lambda})$. The single scattering albedo of the scattering layer is equal to

$$\omega'_0(\tilde{\lambda}) = \frac{\sum_c \omega'_{0,v}(\tilde{\lambda})\ \tau'_v(\tilde{\lambda})}{\tau'_a(\tilde{\lambda})} \tag{17}$$

and the layer average phase function

$$\Phi'(\tilde{\lambda},\Omega_g) = \frac{\sum_c \Phi'_v(\tilde{\lambda},\Omega_g)\ \tau'_v(\tilde{\lambda})}{\tau'_a(\tilde{\lambda})}\ . \tag{18}$$

3.5 Gaseous layer properties

It is assumed that only molecular absorption is taking place in the gaseous layer. The height of level z_a is used to partition the Total Column Water Vapour (TCWV) and Total Column Ozone (TCO3) concentration in each layer assuming a US76 standard atmosphere vertical profile. In addition to H2O and O3, the FASTRE model accounts for the following molecules: CO2, CH4, N2O, CO, and O2. These latter molecules are assumed well-mixed. T_{L_g} denotes the total transmission of that layer.

3.6 Forward model gradients

The derivatives $\mathbf{K}_x$ (Jacobian matrix) with respect to the forward model $y_m(\mathbf{x}, \mathbf{b}; \mathbf{m})$ are calculated as forward finite differences.

3.7 State vector

The state parameters defining the radiative properties of the observed medium are divided into two categories. The first one, noted $\mathbf{x}$, represents the state variables that are retrieved from the observations $\mathbf{y}_{\Omega\tilde{\Lambda}}$ and is referred to as the *state vector*. The second one, noted $\mathbf{b}$, represents those parameters that also have a non-negligeable radiative effects on the observed medium but may not be reliably estimated from those measurements. They are referred to as the *model parameters* and are obtained from external source of information. The size of the state vector is noted n_x.

The state vector $\mathbf{x}$ is composed of the parameters $\mathbf{x}_s$ defining the surface reflectance $r_s(\mathbf{x}, \mathbf{b}; \mathbf{m})$ in the SLSTR bands and the optical thickness associated to each vertex τ_v. The model parameters are composed of the ozone U_{O_3}, water vapour total column content U_{H_2O}, surface pressure P_{z_0}, surface wind speed v_{z_0} and direction v_ϕ, and scattering layer height z_a.

$$\mathbf{b} = \left\{ U_{O_3}, U_{H_2O}, P_{z_0}, v_{z_0}, v_\phi, z_a \right\}. \tag{19}$$

The CISAR algorithm accounts for methane absorption in SLSTR band S6. However a fixed value is used and a possible improvement would be to use an existing methane concentration climatology.

The model parameters are composed of the ozone U_{O_3}, water vapour total column content U_{H_2O}, surface pressure P_{z_0}, surface wind speed v_{z_0} and direction v_ϕ, aerosol layer height z_a.

$$\mathbf{b} = \left\{ U_{O_3}, U_{H_2O}, P_{z_0}, v_{z_0}, v_\phi, z_a \right\}. \tag{20}$$

Surface pressure, water vapour, ozone total column content and surface wind speed and direction are taken from European Centre for Mid-Range Weather Forecasts (ECMWF) data.

4 ALGORITHM DESCRIPTION

4.1 Outline

The CISAR algorithm is composed of the following major steps:

1. **Pre-processing**
   A series of pre-processing operations are performed prior to the inversion. The primary purpose of this pre-processing is the accumulation of SLSTR data during a given period to form a multi-angular observation vector. During the pre-processing, ancillary information required for the inversion and perform some additional computations such as observation uncertainty estimation and prior information definition is also collected. These pre-processing steps are:

   (a) Input data accumulation (Section 4.2)
   In this step, all information needed to perform the inversion is collected and accumulated. For each pixel, SLSTR radiances are accumulated during several days together with requested ancillary information such as the cloud mask, the total gaseous amount, the geometry, band irradiance and finally all relevant information for the computation of the radiometric uncertainties.

   (b) *a priori* information definition (Section 4.2.3)
   The *a priori* information is taken from the retrieval of the previous accumulation periods or from default values when the processing is initiated.

   (c) Measurement noise estimation (Section 4.2.4)
   The radiometric noise of the observation vector is estimated.

2. **Angular and Spectral Inversion**
   The angular and spectral inversion for the retrieval of the aerosol and surface reflectance properties is performed individually for every processed pixel.

   (a) Filtering (Section 4.3.1)
   Observations are filtered according to the acquisition geometry (observations acquired with a VZA or SZA larger than 70°are discarded), TOA BRF validity (observations showing a TOA BRF lower than 0. are discarded) and sun glint condition (over water).

   (b) Inversion (Section 4.3.2.1)
   The state vector is estimated from the measurement vector. The forward model is estimated at each inversion step.

   (c) Retrieval uncertainty estimation (Section 4.3.4)
   The uncertainty of the retrieved solution is estimated.

   (d) Quality control (Section 4.3.3)
   A quality indicator based on factors such as the magnitude of the Jacobians of the AOT/COT and the retrieval uncertainty is calculated.

3. **Product generation** (Section 4.4)

The CISAR algorithm retrieval is delivered in daily products. Each product includes the aerosol and cloud single scattering properties (optical thickness, single scattering albedo and asymmetry factor), in all processed SLSTR bands, the aerosol fine mode and ice cloud fractions, the BiHemispherical Reflectance (BHR) in each band and the QI.

4.2 Pre-processing

This module collects all the information needed to perform the inversion. These data are listed in Section (6).

4.2.1 SLSTR observations

The observation information consists of all available daylight images acquired under different illumination conditions in the S1, S2, S3, S4, S5, S6μm SLSTR bands. SLSTR observations are calibrated according to the official ESA recommendation (Smith 2020):

View	S1	S2	S3	S4	S5	S6
Nadir	0.97	0.98	0.98	1.00	1.11	1.13
Oblique	0.94	0.95	0.95	1.00	1.04	1.07

These observations are accumulated during a period of N_d days to form a multi-angular observation vector. SLSTR acquires radiances $R(\Omega_0, \Omega_v, \tilde{\lambda}, z_s, \mathbf{p})$ with the geometry $\Omega = (\Omega_0, \Omega_v)$ in a spectral interval $\tilde{\lambda}$ when the radiometer is viewing a pixel $\mathbf{p}$ on the Earth from the level z_s. Only observations acquired with sun and viewing zenith angles smaller than $\theta_{\max}$ (reported in Section 6.1) are considered.

The accumulation period is characterized by a time length of N_d days which is shifted by N_s days, as shown in Figure 4. The values of N_d and N_s are reported in Section 6.1. This allows a good trade-off between the need to accumulated multi-angular observations and capture possible variations of the surface, which is assumed temporally invariant during the accumulation period. This features is particular important when few observations per accumulation period are available which require to increase the length of the accumulation period.

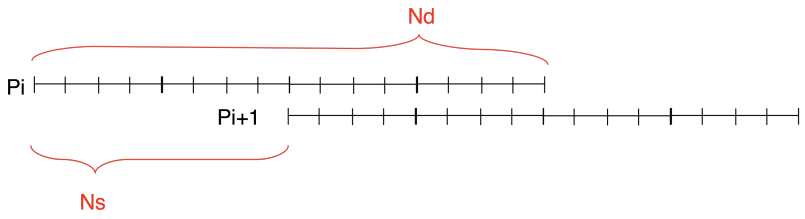

Figure 4: Definition of accumulation periods of N_d days which is shifted by N_s days.

For the purpose of the retrieval process, these radiances are converted into BRF with

$$\mathbf{y}(\Omega_0, \Omega_v, \tilde{\lambda}, \mathbf{p}) = \mathbf{y}(t, \tilde{\lambda}, \mathbf{p}) = \frac{\pi\, R(\Omega_0, \Omega_v, \tilde{\lambda}, z_s, \mathbf{p})\, d_{\odot}^2(t)}{E_0(\tilde{\lambda}, z_s)\, \mu_0} \tag{21}$$

where $d_{\odot}$ is the Sun-Earth distance at time t in Astronomical Unit (AU) and $E_0(\tilde{\lambda})$ is the exo-atmospheric solar irradiance in the SLSTR channel $\tilde{\lambda}$. $\{\Omega_0, \Omega_v, \tilde{\lambda}, z_s, \mathbf{p}\}$ constitute the independent parameters determining the observation conditions and are denoted $\mathbf{m} = \{\Omega_0, \Omega_v, \tilde{\lambda}, z_s, \mathbf{p}\}$.

For a given band, all observations sequentially accumulated during N_d days to form a virtual multi-angular observation system. The corresponding measurement vector is noted

$$\mathbf{y}_{\Omega}(\tilde{\lambda}, z_s, \mathbf{p}) = \mathbf{y}_m(\Omega_0(t_1), \cdots, \Omega_0(t_N), \Omega_v, \tilde{\lambda}, z_s, \mathbf{p}) = \mathbf{y}_m(t_1, \cdots, t_N, \Omega_v, \tilde{\lambda}, z_s, \mathbf{p}) = \mathbf{y}_{\Omega\tilde{\lambda}}(\Omega_v, z_s, \mathbf{p}). \tag{22}$$

To avoid coregistration issues between the nadir and the oblique view, SLSTR observations are aggregated at 10 km resolution super-pixels. The observations are reprojected on a fixed geographical lat/lon grid with fixed 10 km sampling distance between adjacent pixels. The aggregation is done as follows, according to its cloud summary flag:

- if the 80% of sub-pixels are cloud free only cloud-free observation are aggregated and the cloud mask is set to 0.
- if the 80% of sub-pixels are cloudy only cloudy observation are aggregated and the cloud mask is set to 1.
- Otherwise, all pixels are aggregated and cloud mask is a number between 0 and 1 indicating the percentage of cloudy pixels.

4.2.2 Model parameters

The model parameters $\mathbf{b} = \left\{U_{O_3}, U_{H_2O}, P_{z_0}, v_{z_0}, v_{\phi}, z_a\right\}$ are first interpolated into the satellite projection. The following fields undergo additional processing:

U_{H_2O} TCWV is provided at the sea level z_0. The actual TCWV is rescaled at the actual pixel elevation z_p as follows:

(a) Retrieve the geopotential elevation from interpolated ECWMF data.

(b) Calculate the TCWV using the FASTRE standard vertical profile and geopotential height as follows:

$$TCWV = \Sigma_{l=1}^{N_l} q_{H_2O(l)} h(l) \rho_{molH_2O} 10^6 \tag{23}$$

where $q_{H_2O(l)}$ is the water vapour standard profile, $h(l)$ is the standard altitude profile, ρ_{molH_2O} is the water molecular weight and N_l is the level of the standard altitude profile closer to the geopotential elevation.

(c) Determine a rescaled water vapour profile using the retrieved TCWV and the calculated TCWV:

$$q'_{H_2O(l)} = q_{H_2O(l)} \frac{TCWV_{ECMWF}}{TCWV} \tag{24}$$

(d) Use the rescaled profile and the actual pixel elevation to determine the actual TCWV:

$$TCWV' = \Sigma_{l=1}^{N_l} q'_{H_2O(l)} h(l) \rho_{molH_2O} 10^6 \tag{25}$$

where $N(l)$ is the level of the standard altitude closer to the pixel altitude.

P_{z_0} The surface pressure given by the ECWMF data provided at the sea level z_0 is calculated at the actual pixel elevation z_p with

$$P_{z_p} = P_{z_0} * \exp\left(\frac{g\,M\,(z_0 - z_p)}{R_0\,T_{z_0}}\right), \tag{26}$$

g being the Earth-surface gravitational acceleration, M the molar mass of dry air, R_0 the universal gas constant and T_{z_0} the sea level standard temperature.

z_a The aerosol layer height z_a is retrieved from the climatological data set generated by Kinne et al. (2013). This data set provides the vertical profile of extinction coefficient. The aerosol layer height is defined as the elevation corresponding to 80% of the vertical integrated extinction coefficient.

4.2.3 Prior information

4.2.3.1 Prior information on the surface parameter magnitude The prior information $\mathbf{x}_b$ on the state of the surface $\mathbf{x}_s$ is defined from the analysis of the solutions $\hat{\mathbf{x}}(d)$ retrieved during the processing of the previous accumulation period. When CISAR performs a cold start which refers to the processing of the first accumulation period,, the prior information $\mathbf{x}_b$ of $\mathbf{x}_s$ is seasonal climatological values with corresponding uncertainties σ_{x_b}, reported in Section 6.1. This climatology is obtained from MODIS MCD19A3 albedo product (Lyapustin 018b), averaging seasonal data during 10 years (2010 to 2020). The MODIS surface model is the RossThick/Li-Sparse (RTLS, Lucht et al. 2000); to obtain the climatology prior the seasonal RTLS parameters are converted to RPV parameters by inverting the corresponding surface reflectance models. After the processing of the first accumulation period, the prior information $\mathbf{x}_b$ is updated with the *a posteriori* solution. Specifically, the running mean, weighted by the quality indicator, and range in which the parameters vary are estimated based on the previous solutions during a certain time window N_r days long. The value of N_r is reported in Section 6.1. Hence, the prior information $\mathbf{x}_b$ at time t_d the estimation of the prior information $\mathbf{x}_b(t_d)$ and associated uncertainty $\sigma_{x_b}(t_d)$ write

$$\mathbf{x}_b(t_d) = \frac{\sum_{t_i=0}^{t_d-1} \hat{\mathbf{x}}(t_i) QI(t_i)}{\sum_{t_i=0}^{t_d-1} QI(t_i)} \tag{27}$$

$$\sigma_{x_b}(t_d) = \frac{\max_{t_i \in N_r} \hat{\mathbf{x}}(t_i) - \min_{t_i \in N_r} \hat{\mathbf{x}}(t_i)}{2} \tag{28}$$

When not enough solutions $\hat{\mathbf{x}}(t_i)$ are available in the interval N_r, the prior information of the accumulation period t_d and its associated uncertainty are taken from the results of the previous accumulation

period index $t_d - 1$. Such situation will typically occur at the beginning of a processing. If the processing of the last period $t_d - 1$ is successful, the surface prior value at t_d is updated to

$$\mathbf{x}_b(t_d) = \hat{\mathbf{x}}(t_d - 1) \quad (29)$$

$$\sigma_{x_b}(t_d) = \max(\sigma_{\hat{\mathbf{x}}}(t_d - 1), \sigma_{\min}) \quad (30)$$

where $\sigma_{\min}$ (see Section 6.1) is the smallest allowed uncertainty on the surface prior values. Additionally, the update of $\mathbf{x}_b(t_d)$ is constrained by the following conditions

$$\left(\frac{\mathbf{x}_b(t_d)}{t_d}\right)^2 < (\sigma_{\min})^2 \quad (31)$$

When the processing of the previous period is not successful, *e.g.*, there were too few observations, the prior is kept with the same value, *i.e.*, $\mathbf{x}_b(t_d) = \mathbf{x}_b(t_d - 1)$ and the associated uncertainty is set to

$$\sigma_{x_b}(t_d) = \sigma_{x_b}(t_d - 1)\ 1.02^{N_d} \quad (32)$$

such that if this situation lasts several accumulation periods, the uncertainty of $\mathbf{x}_b$ will become larger and larger. The values σ_{x_b} are stored in the $\mathbf{S}_x$ matrix.

4.2.3.2 Prior information on the surface parameter spectral variability The RPV parameters climatology described in Section 4.2.3.1 has been analysed to characterise the spectral variability of the surface parameters in the SLSTR acquisition bands. This spectral constraints are applied to different land covers; however, as snow pixels show a greatly different spectral behaviour, they are excluded from the processing. To identify snowy pixel the normalised-difference snow index (NDSI) is computed from band S1 and S6 (Hall and Riggs 2011). Pixels showing a NDSI larger than 0.75 are classified as now and discarder by the processing. After analysing the RPV climatology, the surface constraints are applied in all bands for k, θ and ρ_c, constricting them to assume similar values (very little variability is observed in the climatology dataset).

The constraints on the ρ_0 parameters, which controls the magnitude of the surface albedo, are set only between bands S1-S2 and S5-S6 according to the following equation:

$$\rho_{0,S1/S5} = a_{S1/S5} \times \rho_{0,S2/S6} + b_{S1/S5} \quad (33)$$

The uncertainty $\sigma_{S1/S5}$ associated to the spectral constraints and the values of $a_{S1/S5}$ and $b_{S1/S5}$ are reported in Section 6.1. Equation 33 is deployed during the inversion to infer a transfer of information from longer wavelengths towards the shorter ones, in this case from band S2 to S1 and from band S6 to S5.

4.2.3.3 Prior information on the aerosol optical thickness The prior information on the magnitude of AOT is taken from a climatology data set prepared by (Kinne et al. 2013), which delivers the aerosol optical thickness annual mean per aerosol type (coarse, fine absorbing, fine non-absorbing). The associated uncertainty in each band is proportional to the prior magnitude and to the TOA BRF:

$$\sigma_{\mathbf{x_b}}(t_d, \lambda) = 20. \times \mathbf{x_b}(t_{d-1}, \lambda) \times \mathbf{y_0}(t_d, \lambda) \quad (34)$$

4.2.3.4 Prior information on the cloud optical thickness The prior information on the magnitude of the COT is built from the TOA BRF spectral acquisition, upon analysis on satellite observation simulations for different COTs with the RTMOM model (Govaerts 2006). Figure 5 shows the TOA BRF simulated with the RTMOM model over a black lambertian surface with ice and liquid water clouds for different COTs. The cloud phase discrimination can thus be built considering the ratio between bands S6 and S1: ice clouds are brighter at shorter wavelengths and darker in band S6, while liquid water clouds show opposite behaviour.

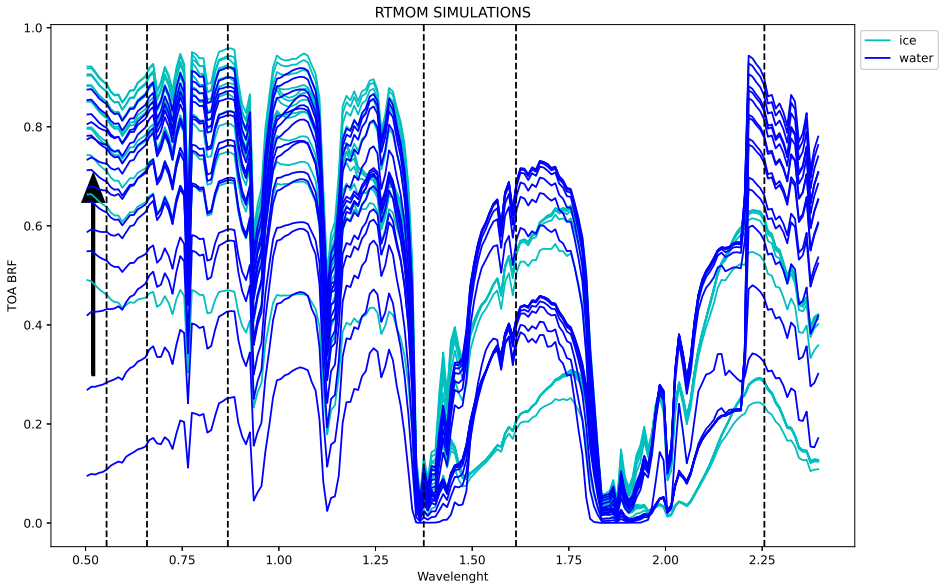

Figure 5: RTMOM simulations over a black lambertian surface for different COTs values. Cyan lines represent ice crystals, blue lines represent liquid water droplets. The black arrow indicates increasing COT.

The prior information on the COT magnitude is built from the ratio between bands S1 and S4 (Fig. 6):

$$\mathbf{x}_b(t) \quad = \quad a \times exp\left(b \times \frac{\mathbf{y}(t, \lambda_{S4}, p)}{\mathbf{y}(t, \lambda_{S1}, p)}\right) \tag{35}$$

where $a = 1.4$ and $b = 35$. The uncertainty on the COT magnitude is equal to the 50% of the prior magnitude, based on an analysis of the algorithm performances over selected well characterised targets.

Over bright surface the discrimination between aerosols and clouds is trickier for CISAR. For this reason a "path" is implement in CISAR: when the ρ_0 prior in band S1 is larger than 0.2 and the TOA BRF in S6 is larger than the one in S1, the pixel is consider cloud free and the prior on the cloud is set to 0.01.

Over water, pixels are classified in 3 categories:

- cloudy: if the TOA BRF in S6 is larger than 0.2.

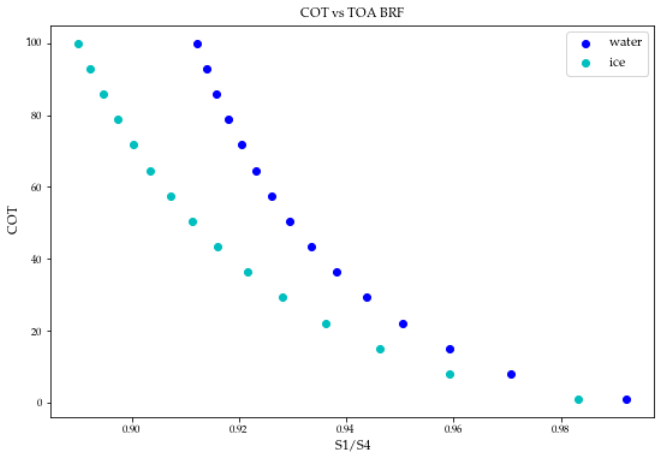

Figure 6: COT magnitude in function of the ratio between the TOA BRF in band S4 and in band S1..

- cloud free: if the TOA BRF in S6 is smaller than 0.01.
- unclear if the TOA BRF in S6 is in between 0.01 and 0.2.

For cloudy (cloud free) pixels the AOT (COT) prior is set to 0.01 with equal uncertainty.

4.2.3.5 Prior information on AOT temporal variability

$$x = X - \overline{X} \tag{36}$$

The variable x is assumed to be a white noise process, so that $E\{x\} = 0$ and $E\{x^2\} = \sigma_x^2$. Assuming that the daily aerosol load variations are represented by a first order auto regressive model, the equation that describes in time the evolution of x can be written

$$x_{t+1} = \alpha\, x_t + \beta \tag{37}$$

where α is the autocorrelation coefficient between time t and $t+1$, derived from AERONET data temporal analysis, and β is a white noise process.

If x_{t_i} is the value of the state variable at time t_i, it is possible to derive the value of x_{t_j} at time t_j by applying recursively Equation (37). It can be easily shown that an expression of an estimate of the difference between x_{t_j} and x_{t_i} can be written as

$$x_{t_j} - x_{t_i} = \left(\alpha^j - 1\right)\; x_{t_i} + \alpha^{j-1} \cdot \beta_1 + \ldots + \beta_j \tag{38}$$

The uncertainty associated to the assumption $x_{t_j} - x_{t_i} = 0$ is defined as

$$\sigma_A^2(t_{i,j}, \tilde{\lambda}) = \left(A_d + \frac{A_a}{1 + \exp(-A_b\,(|t_i - t_j| - A_c))}\right)^2 \tag{39}$$

The values of the coefficients A_a, A_b, A_c and A_d are given in Section (6.1). The elements of $\sigma_A^2(t_{i,j})$ are stored in the $\mathbf{S}_a$ matrix. The resulting model is shown in Figure 7.

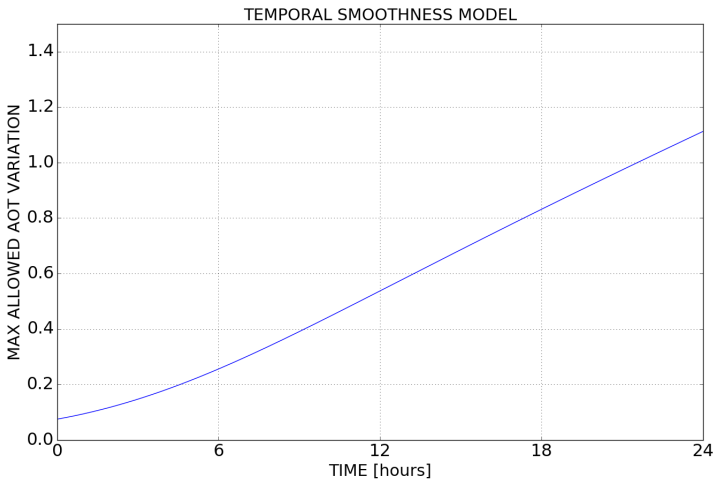

Figure 7: AOT temporal smoothness model.

4.2.3.6 Prior information on AOT/COT spectral variability Similarly, constraints on the spectral variability of the AOT/COT can be used as suggested by Dubovik et al. (2011). This dependency is used to determine the correlation of $\tau_a(\tilde{\lambda})$ between bands $\tilde{\lambda}_i$ and $\tilde{\lambda}_j$. Within a pre-defined aerosol/cloud class c, we have

$$\tau_c(\tilde{\lambda}_i) = \tau_c(\tilde{\lambda}_j)\ \frac{\sigma_e(\tilde{\lambda}_i)}{\sigma_e(\tilde{\lambda}_j)} \tag{40}$$

where σ_e is the extinction coefficient. As each optical thickness in each processed spectral band $\tilde{\lambda}$ for a given aerosol class is retrieved independently, the spectral variation of τ_c is constrained assuming that the retrieved optical thickness $\tau_c(\tilde{\lambda}_i)$ in band $\tilde{\lambda}_i$ could be related to the one in band $\tilde{\lambda}_j$ with Equation (40) assuming an σ_L depending on the particle class, chosen by analysing the algorithm performances over selected well characterised targets varying σ_L. The values of σ_L for each atmospheric particle are reported in Section 6.1.

4.2.3.7 Prior information on AOT spatial variability Aerosol load is assumed to be spatially smooth. To exploit this assumption while keeping the processing of each pixel independent (to allow better parallelism of the inversion), within the overlap between two accumulation period (see Figure 4) the AOT solution retrieved in one accumulation period is used to build the prior information for the next period. In particular, for each solution retrieved during the period P_i at pixel **p** a weighted mean where the distance from the central pixel is the weight is computed over the surrounding $N_p \times N_p$ pixels and used as prior information for the same pixel at the period P_{i+1}.

The uncertainty associated with this prior information is defined as in Eq. 34.

4.2.4 Measurement system uncertainty

A reliable estimation of the measurement system uncertainty is one of the most critical aspects of the CISAR algorithm as it strongly determines the likelihood of the solution. The measurement system

total error covariance matrix $\mathbf{S}_y$ is composed of

$$\mathbf{S}_y = \mathbf{S}_N + \mathbf{S}_B + \mathbf{S}_F \tag{41}$$

with

S_N the radiometric noise matrix;

S_B the equivalent model parameter noise matrix;

S_F the forward model uncertainty matrix.

All uncertainties are expressed in BRF. The elements i, j of $\mathbf{S}_y$ of dimensions $m \times m$, where m is the number of elements of the observation vector, are composed of

$$\mathbf{S}_y(i,j) = \begin{pmatrix} \sigma^2(\bar{t}_0,\tilde{\lambda}_1) & r_{12}\sigma(\bar{t}_0,\tilde{\lambda}_1)\sigma(\bar{t}_1,\tilde{\lambda}_1) & \cdots & r_{1N}\sigma(\bar{t}_0,\tilde{\lambda}_1)\sigma(\bar{t}_N,\tilde{\lambda}_1) & r_{1N+1}\sigma(\bar{t}_0,\tilde{\lambda}_1)\sigma(\bar{t}_1,\tilde{\lambda}_2) & \cdots & r_{1M_y}\sigma(\bar{t}_0,\tilde{\lambda}_1)\sigma(\bar{t}_N,\tilde{\lambda}_3) \\ r_{21}\sigma(\bar{t}_1,\tilde{\lambda}_1)\sigma(\bar{t}_0,\tilde{\lambda}_1) & \sigma^2(\bar{t}_1,\tilde{\lambda}_1) & \cdots & \cdots & \cdots & \cdots & r_{2M_y}\sigma(\bar{t}_1,\tilde{\lambda}_1)\sigma(\bar{t}_N,\tilde{\lambda}_3) \\ \vdots & \cdots & \ddots & \cdots & \cdots & \cdots & \vdots \\ r_{2M_y}\sigma(\bar{t}_0,\tilde{\lambda}_1)\sigma(\bar{t}_N,\tilde{\lambda}_3) & \cdots & \cdots & \cdots & \cdots & \ddots & \sigma^2(\bar{t}_N,\tilde{\lambda}_3) \end{pmatrix} \tag{42}$$

4.2.4.1 Radiometric uncertainty $\mathbf{S}_N$

The total radiometric uncertainty is composed of

σ_i the instrument radiometric noise;

σ_r the geo-location/coregistration accuracy.

The contribution σ_i is set to a constant value defined as a percentage of the measurement vector $\mathbf{y}_{\Omega\tilde{\Lambda}}$.

The geo-location/coregistration inaccuracies σ_r needs to be estimated for each pixel of an image

$$\sigma_r^2(t,\tilde{\lambda},\mathbf{p}) = \left(\frac{\partial \mathbf{y}(t,\tilde{\lambda},p_x,p_y)}{\partial p_x}\sigma_x(\bar{t},\tilde{\lambda})\right)^2 + \left(\frac{\partial \mathbf{y}(t,\tilde{\lambda},p_x,p_y)}{\partial p_y}\sigma_y(\bar{t},\tilde{\lambda})\right)^2 \tag{43}$$

where $\sigma_{x,y}$ is the geo-location/coregistration standard deviation of channel $\tilde{\lambda}$ acquired at time $\bar{t}$. It is expected that the rectification noise is spectrally correlated but not temporally correlated. Hence the terms of the matrix $\mathbf{S}_N$ writes

$$\mathbf{S}_N(i,j) = \delta(i,j)\sigma_i^2(\tilde{\lambda}) + r_r(i,j)\sigma_r(i)\sigma_r(j) \tag{44}$$

where $\delta(i,j)$ is the Dirac function ($\delta(i,j) = 0$ when $i \neq j$). The rectification correlation r_r is 1 when i and j concern the same SLSTR band and 0 otherwise.

However, as pixels are aggregated at 10 km resolution, the only source of uncertainty that is considered at super-pixels level is the radiometric noise, set to 2% at the super pixel resolution.

4.2.4.2 Equivalent model parameter noise $\mathbf{S}_B$ This noise is due to the uncertainties on $\mathbf{b}(\bar{t})$. It is converted in Equivalent Model Parameter Noise (EQMPN). As this piece of information comes from two independent sources of information, they are supposed not correlated.

$$\sigma_B^2(\mathbf{b};\tilde{\lambda},\Omega_0,\Omega_v) = \left(\frac{\partial y(\mathbf{x},U_{oz};\Omega,\tilde{\lambda})}{\partial U_{oz}}\sigma_{U_{oz}}\right)^2 + \left(\frac{\partial y(\mathbf{x},U_{wv};\Omega,\tilde{\lambda})}{\partial U_{wv}}\sigma_{U_{wv}}\right)^2 \tag{45}$$

The terms of the matrix $\mathbf{S}_B$ write

$$\mathbf{S}_B(i,j) = \delta(i,j)\,\sigma_B^2(\tilde{\lambda},\Omega) \tag{46}$$

4.2.4.3 Forward model uncertainty $\mathbf{S}_F$ This noise results from the fast forward model assumptions and approximations described in Section 3.1. Let $y_R(\mathbf{x},\mathbf{b})$ be an accurate forward model with an explicit representation of the atmospheric vertical profile. A global estimation of this error is performed that does not depend on the actual value of $\mathbf{x}$. The error covariance is

$$\sigma_F^2(\tilde{\lambda},\Omega_0,\Omega_v,\phi) = \left(\mathbf{y}(\Omega,\tilde{\lambda})\right)^2 \frac{1}{N}\sum_{\{\mathbf{x},\mathbf{b}\}}\left(\frac{y_m(\mathbf{x}_\Delta,\mathbf{b}_\Delta,\Omega_\Delta) - y_R(\mathbf{x},\mathbf{b},\Omega)}{y_R(\mathbf{x},\mathbf{b},\Omega)}\right)^2 \tag{47}$$

where $\mathbf{x}_\Delta$ represents the discrete value of $\mathbf{x}$ and $\{\mathbf{x},\mathbf{b}\}$ is the domain of variation of $\mathbf{x}$ and $\mathbf{b}$. The terms of the matrix $\mathbf{S}_F$ writes

$$\mathbf{S}_F(i,j) = \sigma_F^2(\tilde{\lambda},\Omega_0,\Omega_v,\phi) \tag{48}$$

4.3 Angular and spectral inversion

4.3.1 Filtering

The SLSTR observations are considered valid if both viewing and solar zenith angles are smaller than θ_{max}, if the TOA BRF is not negative and, over water, if the geometry does not correspond to sun glint conditions. Over land surfaces, cloudy observations are initially filtered according to the cloud mask to allow the retrieval of the surface and build a good prior on the surface reflectance. Once three accumulation periods are successfully processed, the inversion is performed on both cloudy and cloud free pixels and the cloud mask is no longer used. Over water, the cloud mask is never used and cloudy pixel are always processed.

The size of the measurement vector after screening and data reduction is noted n_y. The maximum size of the measurement vector is set to 20. At high latitude however, multiple observations per day are available. To reduce the size of the observation vector a 2-step filter is applied:

1. In case of more than 2 observations per day, the one with highest BRF in band S1 is discarded, given the higher possibility of being cloudy.
2. If the first step is not enough to reduce n_y, when more than 1 observation per day is available, the one with lowest scattering angle (lowest information content associated to aerosols) is discarded.

4.3.2 Definition of the cost function J

The fundamental principle of optimal estimation is to maximise the probability of the retrieved state conditional on the value of the measurements and any prior information. Formally, it is required to maximise the conditional probability $P = P(\mathbf{x}|\mathbf{y}_{\Omega\tilde{\Lambda}}, \mathbf{x_b}, \mathbf{b})$ with respect to the values of the state vector $\mathbf{x}$ (Section 3.7), where $\mathbf{x_b}$ is the prior value of the state vector (Section 4.2.3) and $\mathbf{b}$ are all the other elements of the radiative transfer, called forward model parameters (Section 3.7). The assumption is made that uncertainties in the measurements ($\mathbf{S}_y$ Equation 41), and prior ($\mathbf{S}_x$) are normally distributed with zero mean. Then, the conditional probability takes on the quadratic form (Rodgers 2000) or (Dubovik et al. 2011):

$$\begin{aligned} P(\mathbf{x}) \quad \propto \quad & \exp\left[-\left(y_m(\mathbf{x},\mathbf{b};\mathbf{m}) - \mathbf{y}_{\Omega\tilde{\Lambda}}\right)^T \mathbf{S}_y^{-1} \left(y_m(\mathbf{x},\mathbf{b};\mathbf{m}) - \mathbf{y}_{\Omega\tilde{\Lambda}}\right)\right] \\ & \exp\left[-\left(\mathbf{x}-\mathbf{x}_b\right)^T \mathbf{S}_x^{-1}\left(\mathbf{x}-\mathbf{x}_b\right)\right] \\ & \exp\left[-\mathbf{x}^T\, \mathbf{H}_a^T\, \mathbf{S}_a^{-1}\, \mathbf{H}_a\, \mathbf{x}\right] \\ & \exp\left[-\mathbf{x}^T\, \mathbf{H}_l^T\, \mathbf{S}_l^{-1}\, \mathbf{H}_l\, \mathbf{x}\right] \end{aligned} \tag{49}$$

where the first two factors represent weighted deviations from measurements and the prior state parameters, respectively, the third the AOT temporal smoothness constraints and the fourth the AOT spectral constraint, with respective uncertainty matrices $\mathbf{S}_a$ and $\mathbf{S}_l$. The two matrices $\mathbf{H}_a$ and $\mathbf{H}_l$, representing respectively the temporal and spectral constraints, can be written as block diagonal matrices

$$\mathbf{H} = \begin{pmatrix} \mathbf{H}^{\rho_0} & \mathbf{0} & \mathbf{0} & \mathbf{0} & \mathbf{0} \\ \mathbf{0} & \mathbf{H}^{k} & \mathbf{0} & \mathbf{0} & \mathbf{0} \\ \mathbf{0} & \mathbf{0} & \mathbf{H}^{\theta} & \mathbf{0} & \mathbf{0} \\ \mathbf{0} & \mathbf{0} & \mathbf{0} & \mathbf{H}^{\rho_c} & \mathbf{0} \\ \mathbf{0} & \mathbf{0} & \mathbf{0} & \mathbf{0} & \mathbf{H}^{\tau} \end{pmatrix} \tag{50}$$

where the four blocks $\mathbf{H}^{\rho_0}$, $\mathbf{H}^{k}$, $\mathbf{H}^{\theta}$ and $\mathbf{H}^{\rho_c}$ express the spectral constraints between the surface parameters. Their values are set to zero when these constraints are not active. The submatrix $\mathbf{H}_a^{\tau}$ can also be written using blocks $\mathbf{H}^{\tau}_{a;\tilde{\lambda},v}$ along the diagonal. For a given spectral band $\tilde{\lambda}$ and aerosol vertex v, the block $\mathbf{H}^{\tau}_{a;\tilde{\lambda},v}$ is defined as follows

$$\mathbf{H}^{\tau}_{a;\tilde{\lambda},v}\, \boldsymbol{\tau}_{\tilde{\lambda},v} = \begin{pmatrix} 1 & -1 & 0 & \dots & \dots \\ 0 & 1 & -1 & 0 & \dots \\ \dots & \dots & \dots & \dots & \dots \\ \dots & \dots & \dots & 1 & -1 \\ \dots & \dots & \dots & \dots & 0 \end{pmatrix} \begin{pmatrix} \tau_{\tilde{\lambda},v,1} \\ \tau_{\tilde{\lambda},v,2} \\ \vdots \\ \tau_{\tilde{\lambda},v,N_t-1} \\ \tau_{\tilde{\lambda},v,1,N_t} \end{pmatrix} \tag{51}$$

In the same way, the submatrix $\mathbf{H}_l^{\tau}$ can be written using blocks $\mathbf{H}^{\tau}_{l;v,t}$. For a given aerosol vertex v

and time t, the block $\mathbf{H}^{\tau}_{l;v,t}$ is defined as follows

$$\mathbf{H}^{\tau}_{l;v,t}\,\boldsymbol{\tau}_{v,t} = \begin{pmatrix} 0 & 0 & 0 & \dots & 0 \\ -\frac{\epsilon_2}{\epsilon_1} & 1 & 0 & \dots & 0 \\ 0 & -\frac{\epsilon_3}{\epsilon_2} & 1 & \dots & 0 \\ \dots & \dots & \dots & \ddots & 0 \\ \dots & \dots & \dots & -\frac{\epsilon_{N_\lambda}}{\epsilon_{N_\lambda-1}} & 1 \end{pmatrix} \begin{pmatrix} \tau_{1,v,t} \\ \tau_{2,v,t} \\ \tau_{3,v,t} \\ \vdots \\ \tau_{N_{\tilde{\lambda}},v,t} \end{pmatrix} \tag{52}$$

where the ϵ_l represents the uncertainties associated with the AOT spectral constraints of the individual vertex v bounding the solution space. Maximising the probability function in Equation (49) is equivalent to minimising the negative logarithm:

$$J(\mathbf{x}) = J_y(\mathbf{x}) + J_x(\mathbf{x}) + J_a(\mathbf{x}) + J_l(\mathbf{x}) + J_s(\mathbf{x}) \tag{53}$$

with

$$J_y(\mathbf{x}) = \left(y_m(\mathbf{x},\mathbf{b},\Omega) - \mathbf{y}_{\Omega\tilde{\Lambda}}\right)\,\mathbf{S}_y^{-1}\,\left(y_m(\mathbf{x},\mathbf{b},\Omega) - \mathbf{y}_{\Omega\tilde{\Lambda}}\right)^T \tag{54}$$

$$J_x(\mathbf{x}) = \left(\mathbf{x}-\mathbf{x}_b\right)\,\mathbf{S}_x^{-1}\left(\mathbf{x}-\mathbf{x}_b\right)^T \tag{55}$$

$$J_a(\mathbf{x}) = \mathbf{x}^T\,\mathbf{H}_a^T\,\mathbf{S}_a^{-1}\,\mathbf{H}_a\,\mathbf{x} \tag{56}$$

$$J_l(\mathbf{x}) = \mathbf{x}^T\,\mathbf{H}_l^T\,\mathbf{S}_l^{-1}\,\mathbf{H}_l\,\mathbf{x} \tag{57}$$

Notice that the cost functio"n J is minimized with respect to the state variable $\mathbf{x}$, so that the derivative of J is independent of the model parameters $\mathbf{b}$ which therefore cannot be part of the solution.

4.3.2.1 Minimization of J This section addresses the problem of the minimization of J, *i.e.*, finding the solution $\hat{\mathbf{x}}$. This is an area where many techniques and methods can be employed and where the tuning of the adopted scheme can turn out to be as important as the scheme itself. Essentially any method of finding the minimum is acceptable in a sense, with the caveat that in an operational context it must be robust and fast. The particular characteristics of this problem are that:

- **First and second derivatives of J (with respect to $\mathbf{x}$) are available and continuous**, which implies that descent algorithms that makes use of the local gradient are possible and these are generally faster than methods that do not.
- **Multiple minima are unlikely** This condition is however not met in the present case, and the solution is searched for different first guess values (see Section 4.3.2.2)
- **J is likely to be approximately quadratic in the region of the solution, far from quadratic elsewhere.** This characteristics is a result of the reasonably strongly non-linear nature of the forward (radiative transfer) problem. It means that quick convergence from a poor starting position is unlikely.

The cost function $J(\hat{\mathbf{x}})$ is minimized, for example using a steepest descent method, or the Levenberg-Marquardt method (combined steepest-descent method / Gauss-Newton method, as described in Section (4.3.2.3)).

The first and second derivatives of J with respect to $\mathbf{x}$ are given by:

$$\mathbf{J}' = \frac{\partial J}{\partial \mathbf{x}} = \mathbf{K}_x^T \mathbf{S}_y^{-1}(y_m(\mathbf{x}, \mathbf{b}, \Omega) - \mathbf{y}_{\Omega\tilde{\Lambda}}) + \mathbf{S}_x^{-1}\ (\mathbf{x} - \mathbf{x}_b) + \mathbf{H}_a^T\ \mathbf{S}_a^{-1}\ \mathbf{H}_a\ \mathbf{x} + \mathbf{H}_l^T\ \mathbf{S}_l^{-1}\ \mathbf{H}_l\ \mathbf{x} \quad (58)$$

$$\mathbf{J}'' = \frac{\partial^2 J}{\partial \mathbf{x}^2} = \mathbf{K}_x^T\ \mathbf{S}_y^{-1}\ \mathbf{K}_x + \mathbf{S}_x^{-1} + \mathbf{H}_a^T\ \mathbf{S}_a^{-1}\ \mathbf{H}_a + \mathbf{H}_l^T\ \mathbf{S}_l^{-1}\ \mathbf{H}_l \quad (59)$$

The expression for $\mathbf{J}''$ is a commonly used approximation in that $\mathbf{K}_x$ is assumed to be independent of $\mathbf{x}$, *i.e.*, the radiative transfer is linear in $\mathbf{x}$. The estimation of the Jacobian matrix $\mathbf{K}_x$ is described in Section (3.6). This is only strictly true near the solution (in the region where J is quadratic) but (see next section), since $\mathbf{J}''$ is only employed near the solution, the approximation is acceptable.

4.3.2.2 First guess The choice of the first guess aims at maximising the convergence speed and avoiding local minimum. Hence it is alternatively set equal to $\pm 50\%$ the prior information for the AOT, and equal to the prior information for the COT and the RPV parameters.

4.3.2.3 Marquardt descent algorithm To find the minimum a "first guess" state vector $\mathbf{x}_0$ is selected as described in Section 4.3.2.2 and proceed with steps $\delta\mathbf{x}_n$, which length decreases when approaching the solution. Assuming the value of J decreases at each step then the updated $\mathbf{x}$ vector is taking the process towards the cost function minimum. The CISAR algorithm relies on the Levenberg-Marquardt method to compute the descent. The use of this algorithm is consistent with the three points made above. The rationale of the Levenberg-Marquardt algorithm is to use a weighted combination of *steepest descent* and *Gauss-Newton descent* according to the characteristics of the cost function. Thus, when the cost function is near quadratic (generally near the solution) the efficiency of the Gauss-Newton algorithm is employed and when the cost function is far from quadratic (generally when far from the solution) the robustness of the Steepest Descent algorithm is favoured.

The Steepest Descent algorithm is intuitively the simplest. The vector $-\mathbf{J}'$ defines the "downward" direction of the local steepest gradient. A move $\delta\mathbf{x} = -\mathbf{J}'$ is almost certainly at least approximately in the direction of the minimum although it may be too far or barely far enough. The step is therefore usually scaled, $\delta\mathbf{x} = -\alpha\mathbf{J}'$ where α is variable. If J is found to be decreasing α can be increased to move faster; if J increases then α is reduced until J decreases. J must eventually decrease with this method otherwise something is wrong with the calculation of $\partial J/\partial\mathbf{x}$. The problem with steepest descent is that it can be very slow to converge, especially near the solution where the gradient necessarily becomes small. It is however, very robust.

The Gauss–Newton method is a modification of Newton's method which is very fast near the solution. The Gauss–Newton method compared to the Newton's method has the advantage that the second derivative of J, which can be challenging to compute, is not required.

The second derivative $\mathbf{J}''$ is calculated only once, after the process of the Levenberg-Marquardt algorithm, to compute the output uncertainties.

The Levenberg-Marquardt inversion algorithm starts with an initialisation to set the cost at the first guess state (see Section 4.3.2.2), $J(\mathbf{x}_0)$, and, normally, to set the initial state for the iteration equal to the first guess, $\mathbf{x}_n = \mathbf{x}_0$.

A maximum number of iterations is permitted, and if no convergence is reached after this number, the algorithm exits at the current state (the iteration count is part of the standard output of the CISAR so that this exit condition can be checked in the results).

4.3.2.4 Inversion constraints During the inversion process, further constraints are applied on the retrieved state variable. For each variable, a validity range is defined; at each iteration every variable is forced to assume values between this range. Also, the retrieval of the AOT in each pixel is dependent on the retrieval of the COT. If the total retrieved COT at observation i for pixel $\mathbf{p}$ is higher than 1.5, then no AOT is retrieved, as the information associated to the aerosol load strongly decreases with respect to the once associated to clouds as the COT increases.

4.3.2.5 Convergence criteria The iteration process is stopped when the decrease in J between iterations, δJ_n is so small as to be negligible or when the number of iterations reaches a maximum threshold defined at the begining of the inversion.

4.3.3 Quality control

The quality of the retrieval depends on several factors related to the dependency of the signal on the variables to be retrieved and to the inversion process. The following parameters are considered for the quality control:

1. **Convervenge**: whether the inversion has reached the maximum number of iterations or not.
2. **Validity range**: whether either the RPV parameters or the AOT assume as values the limit of the validity range. Also, whether the total retrieved COT is higher than 0.5.
3. **Entropy RPV** : the entropy quantifies the information coming from the observations. The entropy for the RPV parameters is calculated as follow:

$$H = -\frac{1}{2}\ln\left(\frac{\sigma_{post}}{\sigma_{prior}}\right) \tag{60}$$

   where σ_{post} is the uncertainty of the solution and σ_{prior} is the uncertainty of the prior information.
4. **Entropy AOT/COT** : same as above but for the AOT or COT.
5. **AOT Jacobian** : it gives information on the dependency of the forward model on the aerosol optical thickness. The magnitude of the Jacobian is weighted by the observation uncertainty.
6. **Residuals** : residuals of the observation term of the cost function.

For each of these fields a test is designed and a quality q_i is assigned. For the convergence $q_i = 0$ when the maximum number of iteration is reached and $q_i = 1$ otherwise. For the validity range, $q_i = 0$ if either the AOT or any of the RPV parameters assume the values at the limit of the validity

range. For all the other fields two thresholds T_1 and T_2 are defined. The following equation is then analysed:

$$s_i T_{i1} \leq p_i(t) \leq s_i T_{i2} \tag{61}$$

where $p_i(t)$ is the value of the parameter p_i for the observation t.When p_i is lower than $s_i T_{i1}$ the corresponding quality q_i is set to 0. When p_i is higher than $s_i T_{i1}$ a quality q_i of 1 is given. When p_i falls within the $[s_i T_{i1}, s_i T_{i2}$ interval, a non-linear model is used to define the test value q_i and range between m_i and 1, where m_i is the minimum value assigned to q_i, allowing to give minimum weight to the different tests.

When all the tests have been performed, the final quality indicator (QI) is computed as follows:

$$\begin{cases} QI = 0, & \text{if } \sum_i (1 - q_i) \geq 1. \\ QI = 1 - \sum_i (1 i q_i) \geq 1, & \text{otherwise.} \end{cases} \tag{62}$$

where i=2,..,5.

4.3.4 Linear error analysis

The retrieval uncertainty is based on the OE theory, assuming a linear behaviour of $y(\mathbf{x}, \mathbf{b})$ in the vicinity of the solution $\hat{\mathbf{x}}$ (Rodgers 2000). Under this condition, the retrieval uncertainty $\sigma_{\hat{\mathbf{x}}}$ is determined by the shape of $J(\mathbf{x})$ in $\hat{\mathbf{x}}$ through the second derivative of the cost function at the solution:

$$\sigma^2_{\hat{\mathbf{x}}} = \left(\frac{\partial^2 J(\mathbf{x})}{\partial \mathbf{x}^2} \right)^{-1} \tag{63}$$

Equation 63 is applied to all the state variables (surface parameters, optical thickness associated to each atmospheric vertex). The uncertainty associated to any quantity $y(\mathbf{x})$ obtained from the state variables (e.g. BHR) is computed considering the cross correlation terms:

$$\sigma^2_{\mathbf{y}} = \sum_i \left[\left(\frac{\partial y(\mathbf{x})}{\partial \mathbf{x_i}} \right)^2 \sigma^2_{\mathbf{x_i}} \right] + \sum_i \sum_{j \neq i} \left[\left(\frac{\partial y(\mathbf{x})}{\partial \mathbf{x_i}} \right) \left(\frac{\partial y(\mathbf{x})}{\partial \mathbf{x_j}} \right) \sigma_{\mathbf{x_i}, \mathbf{x_j}} \right] \tag{64}$$

4.4 Product generation

At the end of the inversion procedure, the products are generated. One product (NetCDF format) is generated daily. As the main focus of the algorithm is the retrieval of aerosols, the aerosol retrievals with QI equal to 0 (bad quality) are not included in the product, while the cloud retrieval is included regardless the QI. If more than one observation per day is present, then only the observation with the highest QI is included in the product. These product data files are named according to the following convention

`YYYYMMDD-ESACCI-L2_AEROSOL-AER_PRODUCTS-SLSTR-SENTINEL_S3A-RAY-vX.X.X.nc`

where

`YYYY`	is the year of the current retrieval
`MM`	is the month of the current retrieval
`DD`	is the day of the current retrieval
`HH`	is the hour of the current retrieval
`mm`	is the minute of the current retrieval
`ss`	is the second of the current retrieval
`X.X.X`	us the version of the algorithm

5 ASSUMPTIONS AND LIMITATIONS

5.1 Assumptions

The CISAR algorithm relies on the following assumptions:

1. Satellite observations are unbiased with an uncertainty characterised by a Gaussian distribution. If this assumption does not hold, the retrieval will also be biased.
2. The radiation regime at the spatial scale of a SLSTR pixel can be represented with a one dimensional horizontally homogeneous RTM. Situations such as aerosol above clouds, broken clouds or non-homogeneous surfaces cannot be accurately represented under this assumption.
3. Topography and slope effects are ignored, *i.e.*, pixels are assumed flat. Given this assumption, the retrieval over mountainous regions might show poorer performances compared to flat pixels.
4. A limited number of aerosol and cloud classes can be used to describe the spectral variability of their properties. The number of classes used in the algorithm limits the atmospheric solution space. If the actual solution lays outside the area delimited by these classes, the solution cannot be found.
5. The surface radiative properties do not change during the course of the accumulation period. This assumption introduces a trade-off when choosing the length of the accumulation period, as the longer the period is, the less valid this assumption is, especially in case of rapidly variant surface reflectance (e.g. snow).
6. The RPV model is considered adequate to accurately represent all types of surface BRF everywhere and all year long at the spatial scale of a SLSTR pixel. This assumption sets a limit of 1km for the spatial resolution. At higher resolutions (*e.g.*500m), the 1D assumption to represent the surface BRF with the RPV model might not be valid anymore.

5.2 Limitations

The following limitations apply to the CISAR algorithm:

1. SLSTR observations are processed only if the corresponding solar and viewing zenith angles are less than 70°.
2. No retrieval will take place if the number of SLSTR observations per channel is smaller than 4.
3. FASTRE only includes one scattering layer. This prevents the determination of the position of the aerosol layer with respect to the clouds.
4. FASTRE is a 1D model, hence any 3D effect cannot be detected.
5. Snow pixels are currently excluded from the processing due to the spectral constraints on the RPV parameters.

6. The surface albedo over water is computed from the wind speed, without taking into account the ocean color. This leads to large AOT overestimation in coastal areas.

6 Input data requirements

6.1 Setup parameters

The following main run-time setup parameters are used within CISAR :

Symbol	**Description**	Default value
	Maximum number of iterations	20
$\theta_{\max}$	Maximum processed sun and viewing zenith angles	70°
A_a	Coefficient of Equation (39)	2.0
A_b	Coefficient of Equation (39)	0.3
A_c	Coefficient of Equation (39)	1.00
A_d	Coefficient of Equation (39)	0.05
N_d	Duration in day of the accumulation period	16
N_s	Duration in day of the shift between two accumulation periods	12
a_{S1}	Coefficient in Eq. 33 for band S1	0.7
b_{S1}	Coefficient in Eq. 33 for band S1	0.0
a_{S5}	Coefficient in Eq. 33 for band S5	0.95
b_{S5}	Coefficient in Eq. 33 for band S5	0.06
σ_{S1}	Uncertainty associated to RPV spectral constraints in band S1	0.01
σ_{S5}	Uncertainty associated to RPV spectral constraints in band S5	0.1
σ_{x_b}	Default uncertainty on the surface parameters	0.03
$\sigma_{\min,RPV}$	Minimum uncertainty on the surface parameters	0.01
$\sigma_{\min,AOT}$	Minimum uncertainty on the surface parameters	0.05
$\sigma_{\max,AOT}$	Maximum uncertainty on the surface parameters	0.25
$\sigma_{L,AOT}$	Uncertainty on AOT spectral relationship defined in Section (4.2.3.6)	1.0
$\sigma_{L,COT}$	Uncertainty on AOT spectral relationship defined in Section (4.2.3.6)	0.5
$\cos g_{\max,}$	Threshold to define sun glint	30
$N_{r,min}$	Minimum duration of the accumulation for the srf prior update	$2 * N_d$
$N_{r,max}$	Maximum duration of the accumulation for the srf prior update	45
N_p	Number of pixels considered in the spatial averaging (Section 4.2.3.7)	3

6.2 Ancillary information

The following ancillary information is requested:

Data	Type	Unit	Description
CMa	Dynamic	N/A	Cloud mask provided from SLSTR input data
TCWV	Dynamic	kg/m^2	Total column water vapour taken from ECMWF reanalysis data, linearly interpolated in time, bilinearly in space
TCO3	Dynamic	Dobson	Total column ozone taken from ECMWF reanalysis data, linearly interpolated in time, bilinearly in space
SRFP	Dynamic	hPa	Surface pressure taken from ECMWF reanalysis data. Surface pressure is calculated from a standard value of 1013.25 hPa at sea level and is converted to pressure at a certain height, using a conversion formula of Plummer et al. (2003).
SWS	Dynamic	m/s	Surface wind speed taken from ECMWF reanalysis data.
SWD	Dynamic	Degrees	Surface wind direction taken from ECMWF reanalysis data.
h	Dynamic	km	Monthly aerosol layer height.
LSM	Static	N/A	Land-sea mask
EVL	Static	m	Pixel elevation

Dynamic data are updated for each processed image. Static data are computed once and for all.

7 ALGORITHM IMPLEMENTATION

This section contains some practical information concerning the implementation of the CISAR algorithm. The systematic processing of SLSTR data is performed using the GEneric DAta Processing Chain (GEDAP) algorithm, whose data flow is described in Section 7.1. GEDAP manages all the I/O for the retrieval algorithms. For this purpose, satellites orbits or images are first decomposed in Tiles if not already available. A *Tile* is defined by a geographical coverage, spatial resolution and geographical projection. Each Tile can be processed independently from the other Tiles. A Tiles has however to be sequentially processed within the defined period.

7.1 Overall GEDAP data flow

The overall GEDAP data flow is presented in Figure (8). The processing is composed of three major modules:

1. **INPUT DATA PREPARATION** In this module, SLSTR images are segmented in Tiles. Count values are converted in TOA BRF and accumulated during N_d days together with all the ancillary information listed in Section (6.2). It also loads the prior information which is set to climatological background values when the first accumulation period is processed.

2. **INVERSION** At the end of the input data preparation, the inversion process takes place for each Tile. The solutions and associated uncertainties are stored in disk files. The prior information on the state of the surface is updated.

3. **PRODUCT GENERATION** When all the Tiles of a given accumulation period are processed, all the Tiles are combined to generate a single full-disk product.

7.2 Input data preparation

For the systematic processing of SLSTR data, images are segmented into tiles composed of 100x100 10km pixels. GEDAP is using netCDF format to manage all the data.

7.2.1 Static Tile

Prior to any other operation, one netCDF file, called Static Tile, is generated, containing immutable data such as latitude, longitude, land/sea mask and pixel elevation.

7.2.2 Input Tiles

SLSTR data are accumulated during the accumulation and stored in Input Tiles . The Input Tiles also host the viewing and illumination angles and the cloud mask.

7.2.3 Prior Tiles

The prior Tiles contains the prior values of the state variables and associated uncertainties.

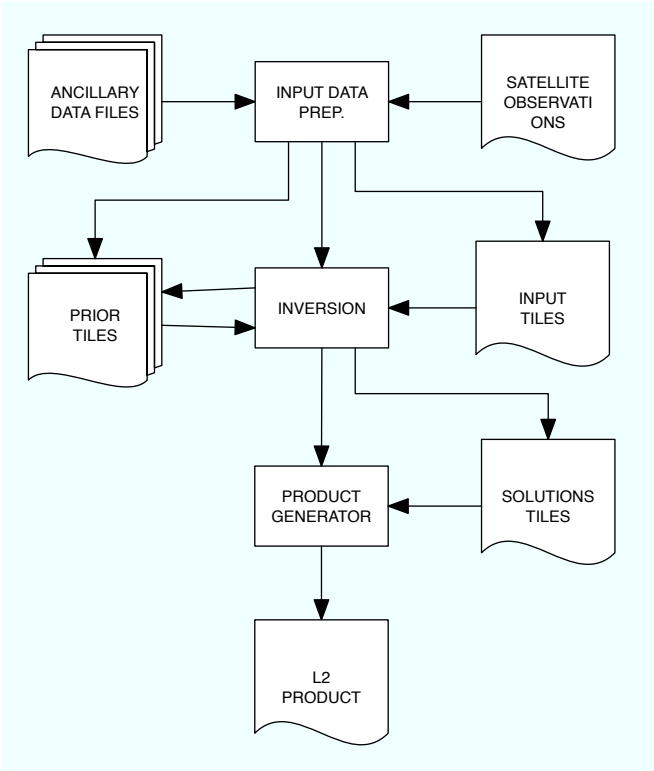

Figure 8: Overall data flow for the processing of SLSTR data. The external data files are the files containing the ancillary information necessary to prepare the input files, together with the satellite data. When all the input files are prepared the inversion takes place. At the end of the inversion the prior is updated and the solution uncertainty estimated. The solutions and the relative uncertainties are finally combined to generate a single product.

7.3 Inversion

The inversion module process the input tiles and performs the loop on all the pixels of the input tiles. There is no interactions between adjacent pixels.

7.4 Product generation

At the end of the inversion, all the solution Tiles are combined to generate the final L2 product, described in Section 4.4.

7.4.1 Product data output format

At the end of the inversion procedure, daily products are generated in the NetCDF format. The naming convention is described in Section 4.4. A daily product contains the following fields:

Name	Description
AOD550	Total AOD in layer L_a in SLSTR band S1
AOD670	Total AOD in SLSTR band S2
AOD870	Total AOD in SLSTR band S3
AOD1600	Total AOD in SLSTR band S5
AOD2200	Total AOD in SLSTR band S6
AOD550_uncertainty	Estimated total AOD uncertainty in band S1
AOD670_uncertainty	Estimated total AOD uncertainty in band S2
AOD870_uncertainty	Estimated total AOD uncertainty in band S3
AOD1600_uncertainty	Estimated total AOD uncertainty in band S5
AOD2200_uncertainty	Estimated total AOD uncertainty in band S6
FM_AOD550	Fraction of fine mode AOF in band S1
FM_AOD670	Fraction of fine mode AOD in band S2
FM_AOD870	Fraction of fine mode AOD in band S3
FM_AOD1600	Fraction of fine mode AOD in band S5
FM_AOD2200	Fraction of fine mode AOD in band S6
SSA_aer550	Aerosol SSA in band S1
SSA_aer670	Aerosol SSA in band S2
SSA_aer870	Aerosol SSA in band S3
SSA_aer1600	Aerosol SSA in band S5
SSA_aer2200	Aerosol SSA in band S6
SSA_aer554_uncertainty	Estimated aerosol SSA uncertainty in band S1
SSA_aer670_uncertainty	Estimated aerosol SSA uncertainty in band S2
SSA_aer870_uncertainty	Estimated aerosol SSA uncertainty in band S3
SSA_aer1600_uncertainty	Estimated aerosol SSA uncertainty in band S5
SSA_aer2200_uncertainty	Estimated aerosol SSA uncertainty in band S6
g_aer550	Aerosol asymmetry factor in band S1
g_aer670	Aerosol asymmetry factor in band S2
g_aer870	Aerosol asymmetry factor in band S3
g_aer1600	Aerosol asymmetry factor in band S5
g_aer2200	Aerosol asymmetry factor in band S6
g_aer550_uncertainty	Estimated aerosol asymmetry factor uncertainty in band S1
g_aer670_uncertainty	Estimated aerosol asymmetry factor uncertainty in band S2

g_aer870_uncertainty	Estimated aerosol asymmetry factor uncertainty in band S3
g_aer1600_uncertainty	Estimated aerosol asymmetry factor uncertainty in band S5
g_aer2200_uncertainty	Estimated aerosol asymmetry factor uncertainty in band S6
COD550	Total COD in band S1
COD670	Total COD in band S2
COD870	Total COD in band S3
COD1600	Total COD in band S5
COD2200	Total COD in band S6
COD550_uncertainty	Estimated total COD uncertainty in band S1
COD670_uncertainty	Estimated total COD uncertainty in band S2
COD870_uncertainty	Estimated total COD uncertainty in band S3
COD1600_uncertainty	Estimated total COD uncertainty in band S5
COD2200_uncertainty	Estimated total COD uncertainty in band S6
ICE_COD550	Fraction of ice COD in band S1
ICE_COD670	Fraction of ice COD in band S2
ICE_COD870	Fraction of ice COD in band S3
ICE_COD1600	Fraction of ice COD in band S5
ICE_COD2200	Fraction of ice COD in band S6
SSA_cloud550	Cloud SSA in band S1
SSA_cloud670	Cloud SSA in band S2
SSA_cloud870	Cloud SSA in band S3
SSA_cloud1600	Cloud SSA in band S5
SSA_cloud2200	Cloud SSA in band S6
SSA_cloud550_uncertainty	Estimated cloud SSA uncertainty in band S1
SSA_cloud670_uncertainty	Estimated cloud SSA uncertainty in band S2
SSA_cloud870_uncertainty	Estimated cloud SSA uncertainty in band S3
SSA_cloud1600_uncertainty	Estimated cloud SSA uncertainty in band S5
SSA_cloud2200_uncertainty	Estimated cloud SSA uncertainty in band S6
g_cloud550	Cloud asymmetry factor in band S1
g_cloud670	Cloud asymmetry factor in band S2
g_cloud870	Cloud asymmetry factor in band S3
g_cloud1600	Cloud asymmetry factor in band S5
g_cloud2200	Cloud asymmetry factor in band S6
g_cloud550_uncertainty	Estimated cloud asymmetry factor uncertainty in band S1

g_cloud670_uncertainty	Estimated cloud asymmetry factor uncertainty in band S2
g_cloud870_uncertainty	Estimated cloud asymmetry factor uncertainty in band S3
g_cloud1600_uncertainty	Estimated cloud asymmetry factor uncertainty in band S5
g_cloud2200_uncertainty	Estimated cloud asymmetry factor uncertainty in band S6
BHRiso550	Isotropic BHR in band S1
BHRiso670	Isotropic BHR in band S2
BHRiso870	Isotropic BHR in band S3
BHRiso1600	Isotropic BHR in band S5
BHRiso2200	Isotropic BHR in band S6
BHRiso550_uncertainty	Estimated isotropic BHR uncertainty in band S1
BHRiso670_uncertainty	Estimated isotropic BHR uncertainty in band S2
BHRiso870_uncertainty	Estimated isotropic BHR uncertainty in band S3
BHRiso1600_uncertainty	Estimated isotropic BHR uncertainty in band S5
BHRiso2200_uncertainty	Estimated isotropic BHR uncertainty in band S6
QI	Quality indicator
qi_aot_entropy	Result of quality test on aot entropy
qi_rpv_entropy	Result of quality test on rpv entropy
qi_convergence	Result of quality test on convergence
qi_cost	Result of quality test on cost
qi_jacobian	Result of quality test on jacobian
time	Acquisition time in second since 1st January 1970
surface_type_number	Land/sea flag
latitude	Pixel center latitude in degree
longitude	Pixel center longitude in degree
pixel_corner_latitude1	Latitude 1st corner in degree
pixel_corner_latitude2	Latitude 2nd corner in degree
pixel_corner_latitude3	Latitude 3rd corner in degree
pixel_corner_latitude4	Latitude 4th corner in degree
pixel_corner_longitude1	Longitude 1st corner in degree
pixel_corner_longitude1	Longitude 2nd corner in degree

pixel_corner_longitude1	Longitude 3rd corner in degree
pixel_corner_longitude1	Longitude 4th corner in degree
pixel_number	Pixel number

A Added value of SLSTR dual view

SLSTR dual view capability represents a decisive asset for the joint retrieval of cloud – aerosol and surface properties. A simple case study has been performed to quantify the added value of this dual view, considering a pixel located at 44.083°N, 5.059°E (Carpentras, South of France) and observed under the following geometrical conditions:

Time	2017/9/20 10:07:30
SZA_Nadir	46.12
SAA_Nadir	150.10
SZA_Oblique	45.90
SAA_Oblique	150.89
VZA_Nadir	10.45
VAA_Nadir	71.76
VZA_Oblique	54.93
VAA_Oblique	187.34

Realistic surface reflectance values for that pixel have been derived from MODIS MCD43A1 product and are listed in the following table:

Band	ρ_0	κ	Θ	ρ_c
S1	0.056	0.918	-0.100	0.622
S2	0.061	0.871	-0.076	0.589
S3	0.174	0.875	-0.047	0.705
S4	0.175	0.900	-0.050	0.705
S5	0.175	0.913	-0.061	0.696
S6	0.113	0.927	-0.028	0.836

The following tables show the value Jacobian of FASTRE, the CISAR forward model, for the nadir and oblique view for three different type of scenes: (*i*) cloud free with an aerosol optical thickness of 0.2; (*ii*) water cloud with a COT of 15.0 and (*iii*) ice cloud with a COT of 18.0. These values are taken from the global Optical Thickness (OT) climatology (Bevan et al. 2012 and Pincus 2017).

Table 2: Jacobians for nadir view and AOT=0.2

Band	BRF	ρ_0	κ	Θ	ρ_c	AOT
S1	0.111	1.109	-0.004	-0.109	-0.025	0.047
S2	0.099	1.171	-0.001	-0.130	-0.028	0.051
S3	0.220	1.197	0.005	-0.400	-0.087	0.011
S4	0.019	0.100	0.002	-0.035	-0.008	0.004
S5	0.212	1.201	0.025	-0.413	-0.090	-0.017
S6	0.112	0.987	0.014	-0.229	-0.051	0.022

Table 3: Jacobians for oblique view and AOT=0.2

Band	BRF	ρ_0	κ	Θ	ρ_c	AOT
S1	0.152	1.101	-0.049	-0.132	-0.025	0.062
S2	0.128	1.248	-0.060	-0.172	-0.031	0.071
S3	0.253	1.322	-0.175	-0.547	-0.102	-0.007
S4	0.010	0.054	-0.006	-0.024	-0.004	0.009
S5	0.234	1.314	-0.158	-0.580	-0.105	0.003
S6	0.117	1.025	-0.078	-0.296	-0.057	0.102

Table 4: Jacobians for nadir view and COT=15.0 (Liquid cloud)

Band	BRF	ρ_0	κ	Θ	ρ_c	AOT
S1	0.495	0.305	-0.008	-0.024	-0.006	0.017
S2	0.513	0.302	-0.009	-0.026	-0.007	0.017
S3	0.594	0.336	-0.033	-0.081	-0.021	0.015
S4	0.065	0.007	-0.001	-0.002	-0.001	0.002
S5	0.487	0.153	-0.014	-0.038	-0.010	0.007
S6	0.552	0.174	-0.010	-0.028	-0.008	0.014

Table 5: Jacobians for oblique view and COT=15.0 (Liquid cloud)

Band	BRF	ρ_0	κ	Θ	ρ_c	AOT
S1	0.571	0.219	-0.006	-0.017	-0.005	0.011
S2	0.587	0.219	-0.007	-0.019	-0.005	0.011
S3	0.662	0.248	-0.025	-0.059	-0.016	0.011
S4	0.050	0.028	-0.000	-0.001	-0.000	0.001
S5	0.537	0.107	-0.010	-0.026	-0.001	0.005
S6	0.581	0.124	-0.007	-0.020	-0.005	0.010

Table 6: Jacobians for nadir view and COT=18.0 (Ice cloud)

Band	BRF	ρ_0	κ	Θ	ρ_c	AOT
S1	0.670	0.102	-0.003	-0.008	-0.002	0.011
S2	0.679	0.109	-0.003	-0.009	-0.002	0.011
S3	0.730	0.140	-0.014	-0.033	-0.009	0.011
S4	0.091	0.003	-0.000	-0.001	-0.000	0.002
S5	0.496	0.040	-0.004	-0.010	-0.003	0.003
S6	0.503	0.059	-0.003	-0.010	-0.003	0.005

Table 7: Jacobians for oblique view and COT=18.0 (Ice cloud)

Band	BRF	ρ_0	κ	Θ	ρ_c	AOT
S1	0.683	0.077	-0.002	-0.006	-0.002	0.008
S2	0.694	0.080	-0.003	-0.007	-0.002	0.008
S3	0.747	0.010	-0.011	-0.025	-0.007	0.008
S4	0.063	0.001	-0.000	-0.000	-0.000	0.001
S5	0.508	0.028	-0.003	-0.007	-0.002	0.002
S6	0.485	0.041	-0.002	-0.007	-0.002	0.004

Figure 9 shows the Jacobian of the 4 surface parameters plus the Jacobian of the OT in the S3 SLSTR bands for both the nadir and oblique view corresponding to AOT=0.2 (left panel) and COT=15.0 (right panel). It can be noticed that especially for low values of optical thickness the dual view brings additional information with respect to the nadir view alone. This feature is highlighted in Figure 10 where the effects of an optical thickness increase on the Jacobians are illustrated. The decrease of the Jacobian magnitude as a function of the optical thickness is clearly visible. In this situation, a further increase of the optical thickness will not affect the simulated TOA BRF. Another interesting aspects is the sensibility of the band S4 to water absorption. This band could be used to build the prior information on the cloud phase, i.e., to discriminate between liquid and ice clouds, and to detect thin cirrus.

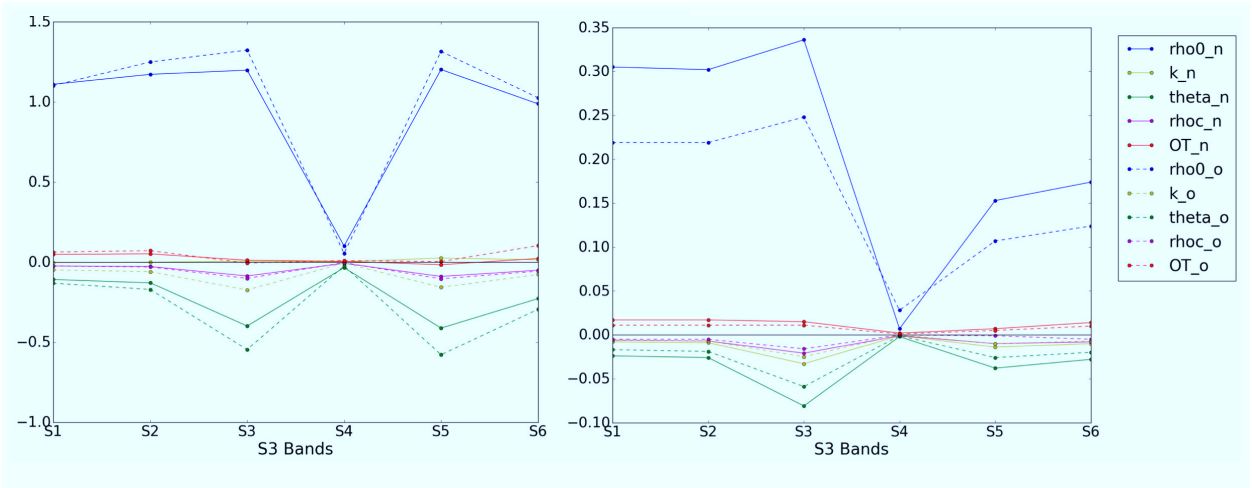

Figure 9: Jacobians of state variables in the S3 bands related to Table 2-3 (left panel) and Table 4-5(right panel). The dashed line represents the oblique view and the solid line the nadir view. It should be noticed that especially for low values of OT (in the left panel AOT=0.2) the oblique view carries more information and can thus facilitate the retrieval.

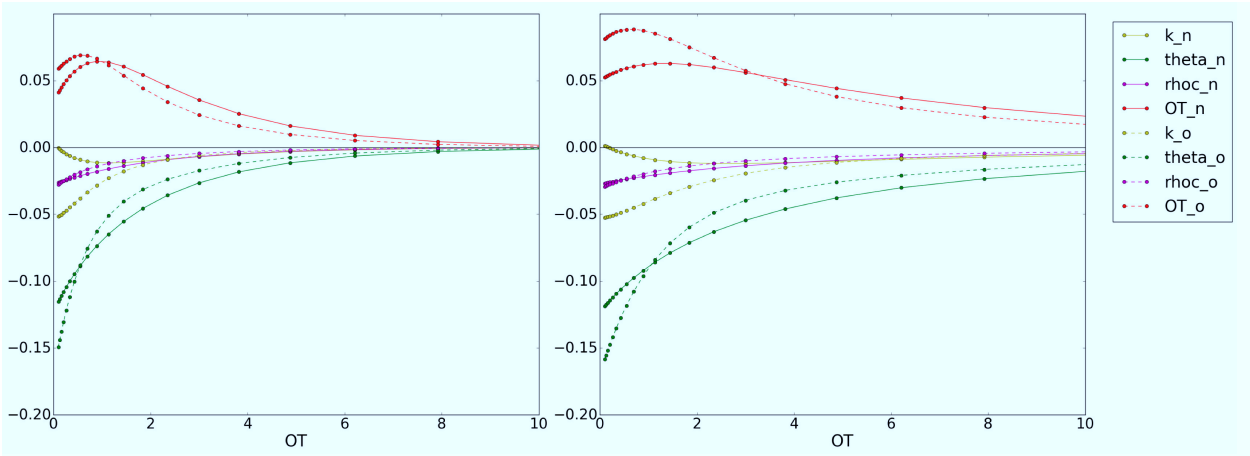

Figure 10: Jacobian of the anisotropy surface parameters (rho0 has not been displayed as the different order of magnitude would make the plot unreadable) and the optical thickness in function of the optical thickness. The dashed line represents the oblique view and the solid line the nadir view. In the left panel and aerosol class is considered for the simulations, while in the right panel a liquid cloud type has been considered. All the plots are displayed at 550 nm.

References

Bevan, S., P. North, S. Los, and W. Grey (2012). A global dataset of atmospheric aerosol optical depth and surface reflectance from aatsr. Remote Sensing of Environment 116, 199–210.

Cox, C. and W. Munk (1954, November). Measurement of the Roughness of the Sea Surface from Photographs of the Sun's Glitter. Journal of the Optical Society of America 44(11), 838–850.

Dubovik, O., M. Herman, A. Holdak, T. Lapyonok, D. Tanré, J. L. Deuzé, F. Ducos, A. Sinyuk, and A. Lopatin (2011). Statistically optimized inversion algorithm for enhanced retrieval of aerosol properties from spectral multi-angle polarimetric satellite observations. Atmospheric Measurement Techniques 4, 975–1018.

Engelsen, O., B. Pinty, M. M. Verstraete, and J. V. Martonchik (1996). Parametric bidirectional reflectance factor models: evaluation, improvements and applications.

Fischer, J. and H. Grassl (1984). Radiative transfer in an atmosphere-ocean system: an azimuthally dependent matrix-operator approach. Applied Optics 23, 1032–1039.

Govaerts, Y. (2006). Rtmom v0b.10 user's manual. Technical report.

Govaerts, Y. and M. Luffarelli (2018, March). Joint retrieval of surface reflectance and aerosol properties with continuous variations of the state variables in the solution space: Part 1: theoretical concept. Atmos. Meas. Tech. 11, 6589–6603.

Govaerts, Y. M., S. Wagner, A. Lattanzio, and P. Watts (2010, January). Joint retrieval of surface reflectance and aerosol optical depth from MSG/SEVIRI observations with an optimal estimation approach: 1. Theory. Journal of Geophysical Research 115(D02203), doi:10.1029/2009JD011779.

Hall, D. K. and G. A. Riggs (2011). Normalized-Difference Snow Index (NDSI). In V. P. Singh, P. Singh, and U. K. Haritashya (Eds.), Encyclopedia of Snow, Ice and Glaciers, pp. 779–780. Springer Netherlands.

Kinne, S., D. O'Donnel, P. Stier, S. Kloster, K. Zhang, H. Schmidt, S. Rast, M. Giorgetta, T. F. Eck, and B. Stevens (2013, December). MAC-v1: A new global aerosol climatology for climate studies. Journal of Advances in Modeling Earth Systems 5(4), 704–740.

Koepke, P. (1984, June). Effective reflectance of oceanic whitecaps. Applied Optics 23(11), 1816.

Liu, Q. and E. Ruprecht (1996). Radiative transfer model: matrix operator method. Applied Optics 35, 4229–4237.

Lucht, W., C. Schaaf, and A. Strahler (2000). An algorithm for the retrieval of albedo from space using semiempirical brdf models. IEEE Transactions on Geoscience and Remote Sensing 38(2), 977–998.

Lyapustin, A., Y. W. (2018b). Mcd19a3 modis/terra+aqua brdf model parameters 8-day l3 global 1km sin grid v006. Technical report.

Morel, A. (1988, September). Optical modeling of the upper ocean in relation to its biogenous matter content (case I waters). Journal of Geophysical Research: Oceans 93(C9), 10749–10768.

Pincus, R. . N. C. f. A. R. S. E. (2017). The climate data guide: Cloud observations from modis.

Plummer, S., J. Chen, G. Dedieu, and M. Simon (2003). GLOBCARBON Detailed Processing Model. Technical Report GLBC-ESL-DPM-V1.3.

Rahman, H., B. Pinty, and M. M. Verstraete (1993). Coupled surface-atmosphere reflectance (CSAR) model. 2. Semiempirical surface model usable with NOAA Advanced Very High Resolution Radiometer Data. Journal of Geophysical Research 98(D11), 20,791–20,801.

Rodgers, C. D. (2000). Inverse methods for atmospheric sounding. Series on Atmospheric Oceanic and Planetary Physics. World Scientific.

Smith, D. (2020). Sentinel-3 slstr vis and swir channel vicarious calibration adjustments. Technical report.

Vermote, E. F., D. Tanre, J. L. Deuze, M. Herman, and J. J. Morcrette (1997). Second simulation of the satellite signal in the solar spectrum, 6s: An overview. IEEE TGARS 35(3), 675–686.

Wiscombe, W. J. (1977). The Delta-M Method: Rapid Yet Accurate Radiative Flux Calculations for Strongly Asymmetric Phase Functions. Journal of Atmospheric Sciences 34, 1408–1422.